

Ultra-dispersive resonator readout of a quantum-dot qubit using longitudinal coupling

Benjamin Harpt,^{1,*} J. Corrigan,^{1,*} Nathan Holman,^{1,†} Piotr Marciniak,¹ D. Rosenberg,² D. Yost,² R. Das,² Rusko Ruskov,³ Charles Tahan,³ William D. Oliver,² R. McDermott,¹ Mark Friesen,¹ and M. A. Eriksson^{1,‡}

¹*Department of Physics, University of Wisconsin, Madison, WI 53706, USA*

²*MIT Lincoln Laboratory, 244 Wood Street, Lexington, MA 02421, USA*

³*Laboratory for Physical Sciences, 8050 Greenmead Dr., College Park, MD 20740, USA*

(Dated: July 15, 2024)

We perform readout of a quantum-dot hybrid qubit coupled to a superconducting resonator through a parametric, longitudinal interaction mechanism. Our experiments are performed with the qubit and resonator frequencies detuned by ~ 10 GHz, demonstrating that longitudinal coupling can facilitate semiconductor qubit operation in the ‘ultra-dispersive’ regime of circuit quantum electrodynamics.

Coupling semiconductor qubits to superconducting resonators using circuit quantum electrodynamics (cQED) techniques is an important element in proposed quantum computing architectures [1, 2]. Transverse coupling schemes based on qubit-resonator photon exchange are conventionally studied for this purpose. However, the transverse interaction becomes weak when the qubit and resonator frequencies are far from resonance, which could constrain operation protocols for large-scale processors. Longitudinal interactions offer an intriguing alternative for quantum coupling, as they do not require frequency resonance [3]. These couplings have attracted growing attention, and although they have recently been observed in semiconductor-qubit systems [4, 5], they have not yet been utilized to extend device functionality. Here, as an initial use case for longitudinal coupling in quantum-dot qubits, we demonstrate excited-state resonator readout and spectroscopy at qubit frequencies far beyond the typical cQED operating range.

Experiments are performed using a Si/SiGe quantum-dot qubit device coupled to an off-chip, TiN microwave resonator. The qubit and resonator are fabricated on separate dies and vertically integrated in a flip-chip architecture, shown in Fig. 1(a) [5, 6]. Figure 1(b) shows a scanning-electron micrograph of a nominally-identical device with a simplified schematic of the measurement circuit. A double quantum dot (DQD) formed under plunger gates P2 and P3 is coupled to the resonator field through capacitance with gate C; the estimated charge-photon coupling rate is $g_c/2\pi \approx 3.2$ MHz.

During experiments, a continuous ac drive is applied to P3 at the resonator fundamental-mode frequency of $\omega_r/2\pi \approx 1.304$ GHz. This drive modulates the DQD energy detuning adiabatically with amplitude $\tilde{\varepsilon}$, activating a dynamic longitudinal coupling with the resonator

photons [3–5, 7]. The effective interaction Hamiltonian is

$$\tilde{H}_{\parallel} = \hbar \tilde{g}_{\parallel}^0 \cos(\omega_r t) \hat{\sigma}_z (\hat{a} + \hat{a}^{\dagger}), \quad (1)$$

where \tilde{g}_{\parallel}^0 denotes the coupling strength, $\hat{\sigma}_z$ is the Pauli z operator in the qubit energy basis, and \hat{a} and \hat{a}^{\dagger} are photon annihilation and creation operators. The coupling \tilde{g}_{\parallel}^0 gives rise to a qubit-state-dependent resonator drive, which can be measured as changes in its stationary field amplitude. Figure 1(c) shows the normalized resonator transmission amplitude A/A_0 measured near the (2,1)-(1,2) interdot charge transition. The axis for DQD detuning ε is indicated, where the total detuning, $\varepsilon(t) = \varepsilon_0 + \tilde{\varepsilon} \cos(\omega_r t)$, includes a dc component ε_0 . The normalization constant A_0 is defined by the transmission level at $\varepsilon_0 \gg 0$. A boost in A/A_0 measured around $\varepsilon_0 = 0$ is a telltale indicator of \tilde{g}_{\parallel}^0 coupling the DQD to the resonator for this measurement configuration, as shown in Ref. [5].

In the following experiments, we operate our device as a quantum-dot hybrid qubit (QDHFQ) [8, 9]. The qubit frequency at $\varepsilon_0 = 0$ in Fig. 1(c) is $\omega_q/2\pi \approx 2\Delta_1/h = 14.6 \pm 1.2$ GHz, where the interdot tunnel coupling Δ_1 is extracted through fits to the resonator transmission peak (see the Supplementary Information [10] for further details). At large $|\varepsilon_0|$, ω_q is set by the left- or right-dot singlet-triplet splitting, E_L or E_R . We measure E_R using time-averaged pulsed-gate spectroscopy [11], with an alternating-voltage waveform applied to P3. Reservoir tunneling resonances for the ground and first-excited states are marked in Fig. 1(c) with yellow and teal circles, respectively. These resonances occur along equipotentials where a dot energy level aligns with the reservoir Fermi energy, as depicted in Fig. 1(d). From the voltage splitting between resonances, we estimate $E_R/h = 34.8 \pm 1.2$ GHz $\approx \omega_q/2\pi$ for $\varepsilon_0 \gg 0$ [10]. We note that the magnitude of $\tilde{\varepsilon}$ is kept much smaller than $\hbar\omega_q$ and all tunnel couplings for our measurements, so the ac drive cannot excite the qubit.

The above measurements demonstrate operation in the ‘ultra-dispersive’ coupling regime, which we define by the condition $g_c \ll \omega_r \ll \omega_q$. Dynamic longitudinal coupling

* These two authors contributed equally to this work. J. Corrigan present address: Intel Technology Research, Intel Corporation, Hillsboro, OR 97124, USA.

† Present address: HRL Laboratories, LLC., 3011 Malibu Canyon Road, Malibu, CA 90265, USA.

‡ maeriksson@wisc.edu

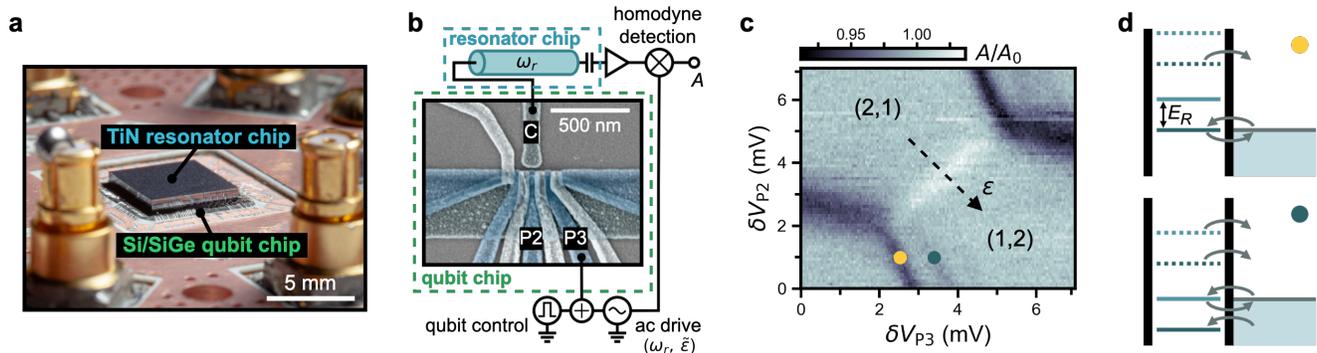


FIG. 1. Pulsed-gate spectroscopy of a 3D DQD-resonator device. (a) Photo of the packaged sample, comprising a Si/SiGe quantum-dot qubit device and TiN microwave resonator integrated in a flip-chip architecture. (b) Simplified circuit schematic for experiments. A false-color, scanning-electron micrograph of a quantum-dot device nominally identical to the one used in experiments is shown. A DQD is formed under gates P2 and P3 and capacitively coupled to the off-chip resonator via gate C. Qubit control pulses and an ac drive at frequency ω_r are applied to P3 (dc voltage sources are not shown). The resonator transmission amplitude A is measured using homodyne detection. (c) Normalized transmission amplitude A/A_0 measured as a function of dc plunger voltages V_{P2} and V_{P3} near the (2,1)-(1,2) charge transition. A pulsed gate voltage is applied for spectroscopy of the right dot. Reservoir tunneling resonances with the lowest two energy states are marked with yellow and teal circles. (d) Energy level configurations corresponding to the equipotentials marked in (c). The dot's energy levels are cycled between lower (solid) and upper (dashed) positions by the alternating-voltage waveform. Arrows indicate electron tunneling pathways between the dot and reservoir.

is an important mechanism for working in this regime; through parametric driving, its coupling strength $\tilde{g}_{\parallel}^0 \propto \tilde{\epsilon}$ can be made significantly larger than effective transverse coupling (which is the dominant qubit-photon interaction for most dispersive-cQED experiments, but considerably weakened at $\omega_q \gg \omega_r$) [5, 12]. In the experiments below, we show how this coupling can be used for QDHQ state readout in the ultra-dispersive regime.

Figure 2(a) illustrates the QDHQ energy levels and a two-step qubit control sequence with fast voltage pulses applied to P3. The logical states $|0\rangle$ and $|1\rangle$ and leakage state $|2\rangle$ are defined as energy eigenstates for the lowest three levels. In the first control step [panel (i)], ϵ_0 is pulsed from ϵ_m to ϵ_p for an interval of $t_{\text{pulse}} = 2$ ns. The detuning amplitude of the pulse is given by $\epsilon_{\text{pulse}} = \epsilon_p - \epsilon_m$. As the pulse shuttles the qubit through the $|0\rangle$ - $|1\rangle$ energy anticrossing at $\epsilon_0 = 0$, fractional excited-state occupation is generated through Landau-Zener transitions [13, 14]. In the second control step [panel (ii)], ϵ_0 is pulsed back to ϵ_m and maintained there for a measurement time of $t_{\text{meas}} = 48$ ns. Qubit-resonator coupling during this interval generates the transmission signal used for readout. We note that no coherent oscillations are observed in our measurements, likely because the manipulation scheme frequently involves idling in the detuning range $\Delta_1 < |\epsilon_0| < E_{L(R)}$, where the qubit is highly susceptible to charge noise [9]. The control protocol can be easily modified to avoid these detuning zones in future experiments.

The above pulse sequence is cycled while simultaneously sweeping dc voltages V_{P2} and V_{P3} near the (2,1)-(1,2) transition. Figures 2(b) and 2(c) show time-

averaged A/A_0 measurements with opposite-amplitude pulses applied, $\epsilon_{\text{pulse}}/h \approx 63$ GHz and -63 GHz, respectively; these amplitudes are indicated by dashed white lines. In both plots, a peak in A/A_0 is visible at $\epsilon_m = 0$ (blue arrows), where the adiabatic qubit modulation near the $|0\rangle$ - $|1\rangle$ anticrossing enlarges \tilde{g}_{\parallel}^0 due to a higher energy curvature [5, 7]. Additional boosts in A/A_0 at $|\epsilon_m| \neq 0$ (yellow and green arrows) are the result of resonator coupling through occupation of the first-excited state. These features are caused by qubit modulation near a $|1\rangle$ - $|2\rangle$ anticrossing at $\epsilon_m = \epsilon_L$ [Fig. 2(c)] or $\epsilon_m = \epsilon_R$ [Fig. 2(d)], activating an excited-state coupling channel, which we label \tilde{g}_{\parallel}^L and \tilde{g}_{\parallel}^R , respectively. DQD-resonator coupling involving excited silicon valley states has been observed previously, but was mediated through the transverse interaction [15]; the A/A_0 peak in our measurements is the key signature of longitudinal coupling.

The resonator transmission signal at ϵ_L or ϵ_R provides a sensitive probe of the qubit state that can be used for readout. Crucially, the $\tilde{g}_{\parallel}^{L(R)}$ coupling channel is only active if the logical state $|1\rangle$ is occupied, which we demonstrate by varying ϵ_{pulse} . Under the model illustrated in Fig. 2(a), excitation into $|1\rangle$ is negligible when the control pulse amplitude is significantly smaller in magnitude than $|\epsilon_{L(R)}|$, preventing interaction with the resonator via $\tilde{g}_{\parallel}^{L(R)}$. The data in Figs. 2(d) and 2(e) are consistent with this model: in contrast to the A/A_0 peak from \tilde{g}_{\parallel}^0 visible at all ϵ_{pulse} , the $|\epsilon_m| \neq 0$ signal boost due to $\tilde{g}_{\parallel}^{L(R)}$ only appears for $\epsilon_{\text{pulse}}/h \gtrsim 13$ GHz in Fig. 2(d) and $\epsilon_{\text{pulse}}/h \lesssim -33$ GHz in Fig. 2(e). A reduction in

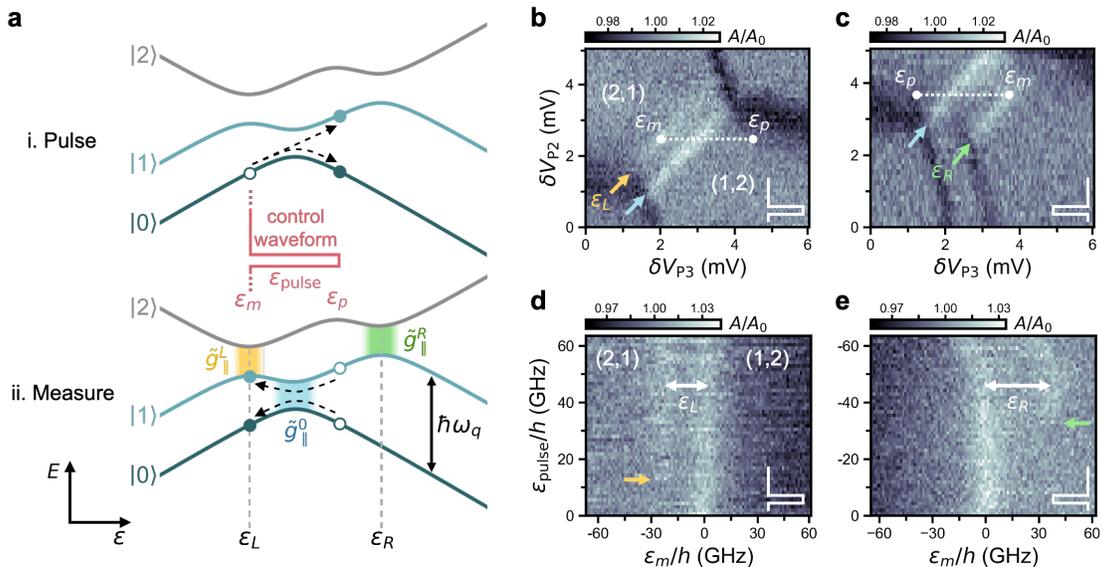


FIG. 2. QDHQ readout and spectroscopy using longitudinal coupling. (a) QDHQ energy level diagram and qubit control scheme. The pulsed voltage waveform is applied to P3. Dashed lines illustrate qubit dynamics and state transitions. (b, c) A/A_0 measured as a function of dc voltages V_{P2} and V_{P3} with positive-amplitude [panel (b)] and negative-amplitude [panel (c)] control pulses applied simultaneously. Dashed white lines indicate the scale of detuning pulses. Signal boosts marked with arrows are from longitudinal coupling at the corresponding-color (blue, yellow, and green) anticrossings in (a). (d, e) A/A_0 as a function of measurement detuning ε_m and pulse amplitude $\varepsilon_{\text{pulse}}$. Arrows highlight $|1\rangle$ -state occupation thresholds. The $|1\rangle$ - $|2\rangle$ energy anticrossing detunings ε_L and ε_R can be estimated from the distance between transmission peaks.

signal for the $|\varepsilon_m| \neq 0$ peaks is also observed near reservoir transition boundaries in Figs. 2(b) and 2(c). Here, reservoir tunneling during the pulse sequence removes occupation from $|1\rangle$, weakening the time-averaged coupling. The qubit-state dependence in these experiments implies that readout can be performed by idling at ε_L or ε_R .

The data in Fig. 2 contain spectroscopic information about the qubit's energy parameters. Using these measurements and additional numerical analysis methods outlined in [10], we are able to reconstruct the full QDHQ Hamiltonian and compute the qubit frequency. We estimate $\omega_q/2\pi = 21.1 \pm 1.2$ GHz and 31.9 ± 3.1 GHz at the ε_L and ε_R readout operating points. This affirms the ultra-dispersive nature of our experiments, since qubit-resonator detuning in this regime, $\Delta = |\omega_q - \omega_r| \sim 2\pi \times 10$ GHz, is orders of magnitude larger than typically used for dispersive-cQED experiments.

The experiments above outline a method for ultra-dispersive QDHQ readout based on longitudinal coupling. Our approach offers a number of potential benefits for qubit operation, which can be explored in future experiments. First, it implements, in principle, a quantum-nondemolition measurement, as \hat{H}_{\parallel} [Eq. (1)] commutes with the qubit Hamiltonian. Second, it requires no qubit-resonator photon exchange, minimizing pathways for Purcell decay [16] and measurement-induced dephasing [17] intrinsic to transverse interactions [3]. Third, our readout is performed at DQD detuning points where qubit relaxation involves a slow spin-flip mechanism,

which may provide a T_1 advantage compared to readout at the $\varepsilon_0 = 0$ measurement point, where no spin flip is required. We emphasize that slow qubit relaxation could be helpful for improving measurement fidelity and achieving single-shot readout in near-term experiments, where relatively weak coupling may necessitate longer integration times. Finally, our technique works in the ultra-dispersive regime, where transverse coupling is suppressed. Our work demonstrates that qubits can be measured through longitudinal interactions while far-detuned from the readout resonator, allowing space for a wide range of qubit frequencies. Longitudinal coupling, therefore, is a promising tool for mitigating engineering bottlenecks and scaling quantum processors.

DATA AVAILABILITY

The data that support the findings of this study are openly available in a [Zenodo repository](#) [18].

ACKNOWLEDGEMENTS

The authors thank HRL Laboratories for support and L.F. Edge for providing the Si/Si_{1-x}Ge_x heterostructure used in this work. This research was sponsored in part by the Army Research Office under Awards No. W911NF-17-1-0274 and No. W911NF-23-1-0110. J.C. acknowl-

edges support from the U.S. National Science Foundation Graduate Research Fellowship Program under Grant No. DGE-1747503 and the Graduate School and the Office of the Vice Chancellor for Research and Graduate Education at the University of Wisconsin-Madison with funding from the Wisconsin Alumni Research Foundation. The authors acknowledge the use of facilities supported by the National Science Foundation through the University of Wisconsin-Madison Materials Research Science and Engineering Center (Grant No. DMR-2309000) and the Major Research Instrumentation (MRI) program (Grant No. DMR-1625348). This material is based in part upon work supported by the Under Secretary of Defense for

Research and Engineering under Air Force Contract No. FA8702-15-D-0001. Any opinions, findings, conclusions or recommendations expressed in this material are those of the author(s) and do not necessarily reflect the views of the Under Secretary of Defense for Research and Engineering and are not necessarily endorsed by nor should they be interpreted as representing the official policies, either expressed or implied, of the Army Research Office or the U.S. Government. The U.S. Government is authorized to reproduce and distribute reprints for U.S. Government purposes notwithstanding any copyright notation herein.

-
- [1] L. Childress, A. S. Sørensen, and M. D. Lukin, “Mesoscopic cavity quantum electrodynamics with quantum dots,” *Phys. Rev. A* **69**, 042302 (2004).
- [2] L. M. K. Vandersypen, H. Bluhm, J. S. Clarke, A. S. Dzurak, R. Ishihara, A. Morello, D. J. Reilly, L. R. Schreiber, and M. Veldhorst, “Interfacing spin qubits in quantum dots and donors—hot, dense, and coherent,” *npj Quantum Inf.* **3**, 34 (2017).
- [3] Andrew J. Kerman, “Quantum information processing using quasiclassical electromagnetic interactions between qubits and electrical resonators,” *New J. Phys.* **15**, 123011 (2013).
- [4] C. G. L. Böttcher, S. P. Harvey, S. Fallahi, G. C. Gardner, M. J. Manfra, U. Vool, S. D. Bartlett, and A. Yacoby, “Parametric longitudinal coupling between a high-impedance superconducting resonator and a semiconductor quantum dot singlet-triplet spin qubit,” *Nat. Commun.* **13**, 4773 (2022).
- [5] J. Corrigan, Benjamin Harpt, Nathan Holman, Rusko Ruskov, Piotr Marciniak, D. Rosenberg, D. Yost, R. Das, William D. Oliver, R. McDermott, Charles Tahan, Mark Friesen, and M. A. Eriksson, “Longitudinal coupling between a Si/Si_{1-x}Ge_x double quantum dot and an off-chip TiN resonator,” *Phys. Rev. Appl.* **20**, 064005 (2023).
- [6] Nathan Holman, D. Rosenberg, D. Yost, J. L. Yoder, R. Das, William D. Oliver, R. McDermott, and M. A. Eriksson, “3D integration and measurement of a semiconductor double quantum dot with a high-impedance TiN resonator,” *npj Quantum Inf.* **7**, 137 (2021).
- [7] Rusko Ruskov and Charles Tahan, “Quantum-limited measurement of spin qubits via curvature couplings to a cavity,” *Phys. Rev. B* **99**, 245306 (2019).
- [8] Zhan Shi, C. B. Simmons, J. R. Prance, John King Gamble, Teck Seng Koh, Yun-Pil Shim, Xuedong Hu, D. E. Savage, M. G. Lagally, M. A. Eriksson, Mark Friesen, and S. N. Coppersmith, “Fast hybrid silicon double-quantum-dot qubit,” *Phys. Rev. Lett.* **108**, 140503 (2012).
- [9] Dohun Kim, Zhan Shi, C. B. Simmons, D. R. Ward, J. R. Prance, Teck Seng Koh, John King Gamble, D. E. Savage, M. G. Lagally, Mark Friesen, S. N. Coppersmith, and Mark A. Eriksson, “Quantum control and process tomography of a semiconductor quantum dot hybrid qubit,” *Nature* **511**, 70 (2014).
- [10] See the Supplementary Information for additional data and explanations of analysis procedures.
- [11] J. M. Elzerman, R. Hanson, L. H. Willems van Beveren, L. M. K. Vandersypen, and L. P. Kouwenhoven, “Excited-state spectroscopy on a nearly closed quantum dot via charge detection,” *Appl. Phys. Lett.* **84**, 4617 (2004).
- [12] Kevin S. Guo, MengKe Feng, Jonathan Y. Huang, Will Gilbert, Kohei M. Itoh, Fay E. Hudson, Kok Wai Chan, Wee Han Lim, Andrew S. Dzurak, and Andre Saraiva, “Methods for transverse and longitudinal spin-photon coupling in silicon quantum dots with intrinsic spin-orbit effect,” [arXiv:2308.12626](https://arxiv.org/abs/2308.12626) (2023).
- [13] J. R. Petta, H. Lu, and A. C. Gossard, “A coherent beam splitter for electronic spin states,” *Science* **327**, 669 (2010).
- [14] Zhan Shi, C. B. Simmons, Daniel R. Ward, J. R. Prance, Xian Wu, Teck Seng Koh, John King Gamble, D. E. Savage, M. G. Lagally, Mark Friesen, S. N. Coppersmith, and M. A. Eriksson, “Fast coherent manipulation of three-electron states in a double quantum dot,” *Nat. Commun.* **5**, 3020 (2014).
- [15] X. Mi, Csaba G. Péterfalvi, Guido Burkard, and J. R. Petta, “High-resolution valley spectroscopy of Si quantum dots,” *Phys. Rev. Lett.* **119**, 176803 (2017).
- [16] A. A. Houck, J. A. Schreier, B. R. Johnson, J. M. Chow, Jens Koch, J. M. Gambetta, D. I. Schuster, L. Frunzio, M. H. Devoret, S. M. Girvin, and R. J. Schoelkopf, “Controlling the spontaneous emission of a superconducting transmon qubit,” *Phys. Rev. Lett.* **101**, 080502 (2008).
- [17] D. H. Slichter, R. Vijay, S. J. Weber, S. Boutin, M. Boissonneault, J. M. Gambetta, A. Blais, and I. Siddiqi, “Measurement-induced qubit state mixing in circuit QED from up-converted dephasing noise,” *Phys. Rev. Lett.* **109**, 153601 (2012).
- [18] “Source data for the publication ‘Ultra-dispersive resonator readout of a quantum-dot qubit using longitudinal coupling,’” [Zenodo](https://zenodo.org/record/12206818) (2024), 10.5281/zenodo.12206818.
- [19] J. P. Dodson, H. Ekmel Ercan, J. Corrigan, Merritt P. Losert, Nathan Holman, Thomas McJunkin, L. F. Edge, Mark Friesen, S. N. Coppersmith, and M. A. Eriksson, “How valley-orbit states in silicon quantum dots probe quantum well interfaces,” *Phys. Rev. Lett.* **128**, 146802 (2022).

SUPPLEMENTARY INFORMATION

These supplemental materials provide additional data and details about the methods used in this work.

SI. QUBIT HAMILTONIAN & LOGICAL STATES

The QDHQ combines the charge and spin degrees of freedom of a three-electron DQD depicted in Fig. S1(a). The DQD is operated with two electrons in one dot and a single electron in the other dot. In the absence of tunnel coupling, the eigenstates of the four-level system pictured can be defined in the charge-spin basis:

$$\begin{aligned} |L, S\rangle &\equiv |S\rangle |\downarrow\rangle; & |L, T\rangle &\equiv \sqrt{\frac{1}{3}} |T_0\rangle |\downarrow\rangle - \sqrt{\frac{2}{3}} |T_-\rangle |\uparrow\rangle; \\ |R, S\rangle &\equiv |\downarrow\rangle |S\rangle; & |R, T\rangle &\equiv \sqrt{\frac{1}{3}} |\downarrow\rangle |T_0\rangle - \sqrt{\frac{2}{3}} |\uparrow\rangle |T_-\rangle. \end{aligned} \quad (\text{S1})$$

In these definitions, $|S\rangle \equiv (|\uparrow\downarrow\rangle - |\downarrow\uparrow\rangle)/\sqrt{2}$ is the spin-singlet state, while $|T_0\rangle \equiv (|\uparrow\downarrow\rangle + |\downarrow\uparrow\rangle)/\sqrt{2}$ and $|T_-\rangle \equiv |\downarrow\downarrow\rangle$ are spin-triplet states of the doubly-occupied dot; $|\uparrow\rangle$ and $|\downarrow\rangle$ denote spin-up and spin-down electrons in the singly-occupied dot.

The bare (i.e., undressed) DQD Hamiltonian in the charge-spin basis is

$$H_q = \begin{pmatrix} \varepsilon/2 & 0 & \Delta_1 & -\Delta_2 \\ 0 & \varepsilon/2 + E_L & -\Delta_3 & \Delta_4 \\ \Delta_1 & -\Delta_3 & -\varepsilon/2 & 0 \\ -\Delta_2 & \Delta_4 & 0 & -\varepsilon/2 + E_R \end{pmatrix}, \quad (\text{S2})$$

where E_L and E_R are the singlet-triplet energy level splittings in the left and right dot, respectively. There are four interdot tunnel coupling parameters which lead to hybridization of the eigenstates in Eq. (S1): Δ_1 for singlet-singlet tunneling; Δ_2 and Δ_3 for singlet-triplet tunneling; and Δ_4 for triplet-triplet tunneling. Figure S1(b) plots the energy levels of H_q as a function of ε for our device, with parameter values derived in the following sections. For this work, we define the qubit logical states $|0\rangle$ and $|1\rangle$ as the lowest two energy eigenstates of H_q [teal-colored energy levels in Fig. S1(b)]. At large DQD detuning, these logical states are asymptotically equal to the basis states in Eq. (S1).

SII. QUBIT SPECTROSCOPY ANALYSIS METHODS

The following sections describe analysis procedures used for estimating the QDHQ energy parameters. Before plotting or analysis, all data are normalized by the constant A_0 , which denotes the transmission amplitude measured

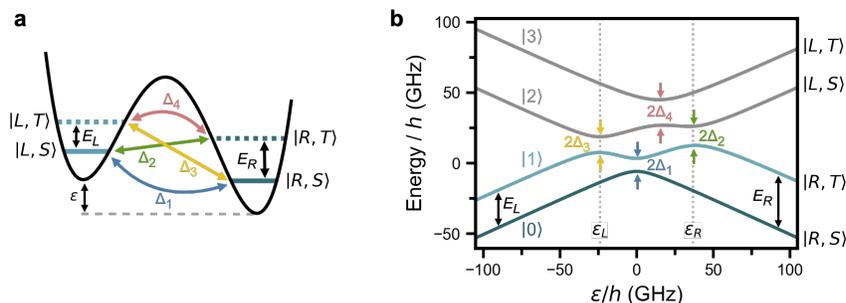


FIG. S1. QDHQ states and energy levels. (a) Electrostatic potential for a three-electron DQD. Quantum-dot energy levels are labeled corresponding to the basis states of Eq. (S1); the third electron's level occupation determines the state of the system in this basis. E_L and E_R denote the singlet-triplet splitting for each dot, and Δ_1 through Δ_4 are interdot tunnel couplings. (b) Energy levels of the system in (a) as a function of ε . Qubit logical-state levels are colored teal. The energy eigenstates $|0\rangle$ through $|3\rangle$ are asymptotically equal to the basis states in Eq. (S1) at large $|\varepsilon|$. Detuning values of the $|1\rangle$ - $|2\rangle$ anticrossings are labeled ε_L and ε_R .

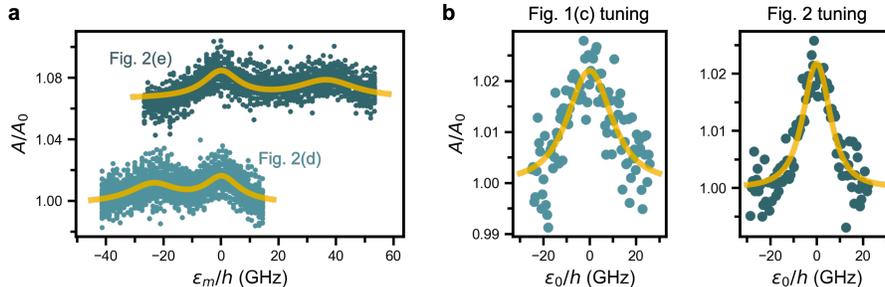


FIG. S2. Curve fitting analysis of resonator transmission peaks. **(a)** Combined traces from Figs. 2(d) (light teal points) and 2(e) (dark teal points; offset for clarity). Yellow curves show phenomenological Lorentzian fits by which ε_L and ε_R are estimated. **(b)** A/A_0 near the (2,1)-(1,2) charge transition measured at the device tunings of Fig. 1(c) (left plot) and Fig. 2 (right plot). Fits using Eq. (S5) are shown as yellow curves.

with the DQD in Coulomb blockade. A_0 is determined independently for each dataset. The estimated values and uncertainties of all parameters are summarized in Table S1 below.

A. Quantum-dot gate lever arms

The device gate lever arms convert changes in gate voltage to calibrated movement of the quantum-dot chemical potentials, and are used throughout the analyses below. We measure gate-to-dot lever arms from the thermal broadening of reservoir tunneling transition lines, as detailed in Ref. [5], obtaining $\alpha_{P2}^L \equiv |\partial\mu_L/\partial V_{P2}| = 0.140 \pm 0.005$ eV/V and $\alpha_{P3}^R \equiv |\partial\mu_R/\partial V_{P3}| = 0.149 \pm 0.003$ eV/V, where μ_L and μ_R are the chemical potentials of the left and right dot. The DQD detuning lever arms for gates P3 and C are calculated using the slopes of reservoir transitions in two-dimensional voltage sweeps:

$$\alpha_{P3}^{\bar{\varepsilon}} \equiv \frac{\partial\varepsilon_0}{\partial V_{P3}} = \alpha_{P3}^R - \alpha_{P2}^L \left| \frac{\delta V_{P2}}{\delta V_{P3}} \right|_L = 0.105 \pm 0.005 \text{ eV/V}; \quad (\text{S3})$$

$$\alpha_C^{\bar{\varepsilon}} \equiv \left| \frac{\partial\varepsilon_0}{\partial V_C} \right| = \alpha_{P2}^L \left| \frac{\delta V_{P2}}{\delta V_C} \right|_L - \alpha_{P3}^R \left| \frac{\delta V_{P3}}{\delta V_C} \right|_R = 0.023 \pm 0.004 \text{ eV/V}. \quad (\text{S4})$$

In these equations, the quantity $|\delta V_i/\delta V_j|_{L(R)}$ represents the slope of a left-dot (right-dot) reservoir transition in (V_j, V_i) parameter space. The values of all lever arms are found to remain roughly constant between the main-text device tunings of Fig. 1(c) and Fig. 2.

B. $|1\rangle$ - $|2\rangle$ anticrossing detunings: $\varepsilon_L, \varepsilon_R$

The detuning values of the $|1\rangle$ - $|2\rangle$ energy anticrossings used for resonator coupling during readout are obtained through phenomenological Lorentzian fits to the data in Figs. 2(d) and 2(e). The data points in Fig. S2(a) show 41 overlaid traces from Fig. 2(d) (light teal) and 25 traces from Fig. 2(e) (dark teal) with $|\varepsilon_{\text{pulse}}|$ beyond the qubit excitation thresholds. The Fig. 2(e) data are vertically offset by $A/A_0 = 0.07$ for clarity, and we have shifted the horizontal positions of traces with $\varepsilon_{\text{pulse}}/h < -57$ GHz to correct for electrostatic device drift during the measurement. The yellow curves are double-Lorentzian fits of each data set; we extract values of $\varepsilon_L/h = -24.0 \pm 1.0$ GHz and $\varepsilon_R/h = 36.7 \pm 1.5$ GHz from the distance between peak centers.

C. Interdot tunnel couplings: $\Delta_1, \Delta_2, \Delta_3$

The interdot tunnel coupling parameter Δ_1 is extracted from measurements of the resonator transmission peak near the (2,1)-(1,2) charge degeneracy point. Figure S2(b) shows two A/A_0 peaks acquired at the same device tunings used for the main-text experiments. We do not apply any control pulses during these measurements; consequently,

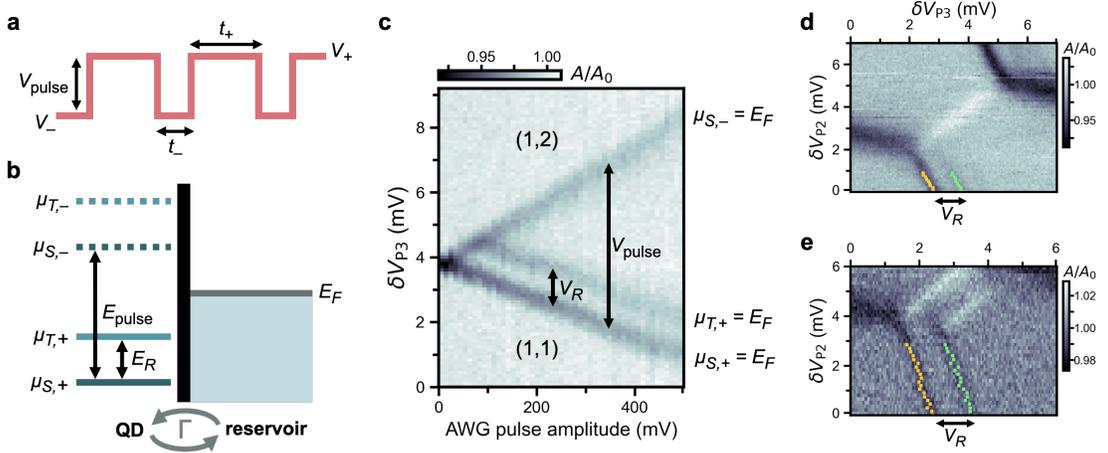


FIG. S3. Pulsed-gate spectroscopy measurement and analysis. (a) Idealized pulsed-voltage waveform applied to gate P3 during measurements. (b) Diagram showing cyclic pulsing of the two lowest right-dot energy levels, split by energy E_R . We label the chemical potential for the spin-singlet ground state $\mu_{S,+}$ during the high-voltage pulse stage and $\mu_{S,-}$ during the low-voltage stage; the spin-triplet, excited-state chemical potential during each stage is $\mu_{T,+}$ and $\mu_{T,-}$. Electrons tunnel cyclically between the dot and neighboring reservoir during pulsing with an overall rate Γ . (c) Typical pulsed-gate spectroscopy measurement: A/A_0 as a function of V_{P3} and AWG pulse amplitude (measured in instrument units). Dips in A/A_0 are caused by resonant electron tunneling. (d) Data from Fig. 1(c) with extracted coordinates for the $\mu_{S,+}$ and $\mu_{T,+}$ tunneling resonances marked with yellow and green points, respectively. The voltage splitting V_R between resonances is used to estimate E_R . (e) Data from Fig. 2(c) with an extended measurement range for the V_{P2} axis. Tunneling resonance coordinates are marked as in (d) and used to estimate E_R .

the DQD remains in its ground state, and can be modeled as a single-electron charge qubit with tunnel coupling t_c . In the following analysis, we assume that t_c is equivalent to the singlet-singlet tunnel coupling Δ_1 of the three-electron QDHF. Following the derivation in Ref. [5], the transmission response for a resonator interacting with the ac-driven charge qubit is given by

$$\frac{A}{A_0} = \frac{1 - \hbar \tilde{g}_{||} / (2\beta \tilde{\epsilon})}{\sqrt{1 + (2\delta\omega/\kappa)^2}}, \quad (\text{S5})$$

where $\tilde{g}_{||} = 4g_c t_c^2 \tilde{\epsilon} / E_{\text{cq}}^3$ and $\delta\omega = 8\hbar g_c^2 t_c^2 / E_{\text{cq}}^3$ are dynamic longitudinal and static dispersive coupling strengths, and $E_{\text{cq}} = \sqrt{\epsilon_0^2 + 4t_c^2}$ is the bare charge qubit energy. The constant β parameterizes direct excitation of the resonator through gate capacitance, and κ is the photon loss rate.

To analyze the data in Fig. S2(b), they are fit using Eq. (S5), with t_c and β as the fitting parameters. The value of $\kappa/2\pi = 125$ kHz is known from resonance linewidth measurements, and the charge-photon coupling rate,

$$\frac{g_c}{2\pi} = \frac{1}{2\pi} \frac{\omega_r \alpha_C^{\tilde{\epsilon}}}{2e} \sqrt{\frac{2Z_r}{\hbar/e^2}} = 3.2 \text{ MHz}, \quad (\text{S6})$$

is calculated using Eq. (S4) and the resonator characteristic impedance, $Z_r \approx 575 \Omega$ [1, 6]. The results are shown by yellow curves in Fig. S2(b), with extracted values of $\Delta_1/\hbar = t_c/\hbar = 7.3 \pm 0.6$ GHz for Fig 1(c) and 4.4 ± 0.2 GHz for Fig. 2.

The transmission peak width scales approximately linearly with t_c in Eq. (S5). Using this relationship, we are able to extrapolate singlet-triplet tunnel couplings for the measurements of Fig. 2 from the known Δ_1 value and the relative peak widths in Fig. S2(a). The values obtained in this manner are $\Delta_2/\hbar = 7.5 \pm 0.6$ GHz and $\Delta_3/\hbar = 6.1 \pm 0.5$ GHz.

D. Right-dot singlet-triplet splitting: E_R (pulsed-gate spectroscopy)

Pulsed-gate spectroscopy is performed by applying an alternating-voltage pulse train to the plunger P3. Figure S3(a) depicts an idealized voltage waveform with peak-to-peak amplitude V_{pulse} and a duty cycle defined by

$D \equiv t_+/(t_+ + t_-)$, where t_+ and t_- are the periods of the high-voltage (V_+) and low-voltage (V_-) pulse stages. The voltage pulses cycle the right-dot energy levels between upper and lower positions separated by $E_{\text{pulse}} = \alpha_{\text{P3}}^R V_{\text{pulse}}$, as diagrammed in Fig. S3(b).

Figure S3(c) shows an illustrative measurement of A/A_0 at the (1,1)-(1,2) reservoir transition as a function of V_{P3} and arbitrary waveform generator (AWG) pulse amplitude. We note that this measurement is acquired at a different device tuning than the main-text experiments, and the microwave resonator drive is delivered through an alternative on-chip port rather than through P3. The duty cycle of the applied pulse train is $D = 0.6$, with $t_+ = 3$ ns and $t_- = 2$ ns. The reservoir energy barrier and pulse-train frequency are calibrated so that the total electron tunneling rate Γ sharply increases at tunings where a dot energy level aligns with the reservoir Fermi energy E_F . The onset of resonant tunneling at these points changes the dot's complex admittance, thereby suppressing A/A_0 . The features in Fig. S3(c) closely resemble those of time-averaged pulsed-gate spectroscopy measurements using conventional integrated charge sensors and lock-in techniques (e.g., Ref [11]). For AWG pulse amplitudes below ~ 100 mV, two tunneling resonances are visible, corresponding to P3 voltages where $\mu_{S,+} = E_F$ and $\mu_{S,-} = E_F$. The splitting between these features provides a direct measurement of the on-chip amplitude V_{pulse} . At larger amplitudes, the pulse window straddles the first-excited energy level, and a third resonance, corresponding to $\mu_{T,+} = E_F$, is observed. The singlet-triplet splitting,

$$E_R = \mu_{T,+} - \mu_{S,+} = \alpha_{\text{P3}}^R V_R, \quad (\text{S7})$$

may be estimated from this measurement using the voltage splitting V_R between the $\mu_{S,+}$ and $\mu_{T,+}$ tunneling resonances.

The pulse train applied in Fig. 1(c) of the main text is configured with $V_{\text{pulse}} \approx 1.7$ mV, $t_+ = 15$ ns, and $t_- = 2$ ns. (As an aside, we speculate that no A/A_0 boost from the \tilde{g}_{\parallel}^R resonator coupling is observed in this experiment because the duty cycle $D = 0.88$ is too small to provide sufficient signal integration time at ε_R .) To estimate E_R , voltage coordinates of the tunneling resonances are extracted using phenomenological double-Lorentzian fits. These coordinates are overlaid on the measurement data in Fig. S3(d), with yellow pixels corresponding to the $\mu_{S,+}$ resonance and green pixels corresponding to the $\mu_{T,+}$ resonance. The $\mu_{S,-}$ resonance is faintly visible as well. We estimate $V_R = 0.97 \pm 0.03$ mV from the average voltage splitting between resonance coordinates, which equates to $E_R = 34.8 \pm 1.2$ GHz using Eq. (S7).

Reservoir tunneling resonances are also observed in the lower part of Fig. 2(c). The control pulse waveform used for this readout experiment has a very large duty cycle of $D = 0.96$, with $t_+ = t_{\text{meas}} = 48$ ns and $t_- = t_{\text{pulse}} = 2$ ns. Only the resonances associated with $\mu_{S,+}$ and $\mu_{T,+}$ tunneling are visible due to the extreme duty cycle. Figure S3(e) shows the same measurement as Fig. 2(c), but with an extended V_{P2} sweep range. We extract $V_R = 1.15 \pm 0.08$ mV and $E_R = 41.3 \pm 2.9$ GHz from the tunneling resonances using the analysis method described above. This E_R value is larger than the value measured in Fig. S3(d). The discrepancy is likely due to variation in electrostatic device tuning between the measurements; singlet-triplet splitting has been shown to change substantially as a function of quantum-dot confinement and lateral position due to local interface disorder [19].

Finally, we note that we are only able to implement pulsed-gate spectroscopy for the right quantum dot in this device, as the left-dot plunger P2 is not connected to coaxial wiring for high-frequency pulsing. The left dot's singlet-triplet splitting E_L is therefore estimated based on other measurement data and numerical calculations described in the next section.

E. Other Hamiltonian parameters: E_L , Δ_4

The main-text experiments do not provide direct measurements of the left-dot singlet-triplet splitting E_L or the triplet-triplet tunnel coupling Δ_4 . However, we are able to estimate these parameters through numerical analysis. We first diagonalize the qubit Hamiltonian in Eq. (S2) as a function of E_L and Δ_4 with the other matrix entries fixed to the values derived above. Then, we compute the $|1\rangle$ - $|2\rangle$ energy anticrossing detunings ε_L and ε_R for each diagonalized matrix and compare them to the experimentally measured values. Figure S4(a) summarizes the results of this analysis, with color-filled contours bounding the regions of (E_L, Δ_4) parameter space in which the calculated ε_L and ε_R values match experimental results to within 1σ or 2σ experimental uncertainty. The closest match to our measurements occurs at the coordinate pair marked with an 'x' in the plot; from these coordinates, we estimate the qubit parameters in the Fig. 2 measurements to be $E_L/h = 27.3 \pm 1.0$ GHz and $\Delta_4/h = 9.3 \pm 1.8$ GHz (the uncertainties are given by the 1σ contour dimensions about this point).

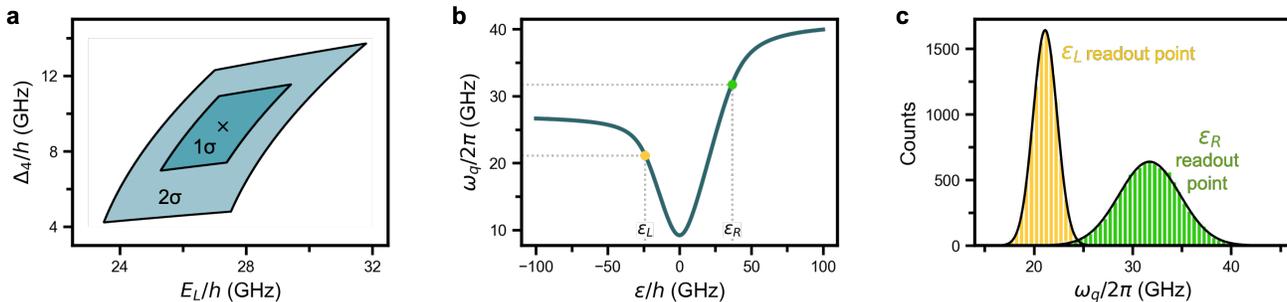


FIG. S4. Qubit spectroscopy numerical analysis. **(a)** Contours showing regions of (E_L, Δ_4) parameter space in which calculated ε_L and ε_R values match Fig. 2 measurements to within 1σ or 2σ experimental uncertainty. The closest-match parameter coordinates marked with an ‘x’ are used as E_L and Δ_4 estimates for main-text experiments. **(b)** Qubit frequency ω_q as a function of ε . Yellow and green circles mark frequencies at the ε_L and ε_R readout operating points. **(c)** Results of a Monte Carlo simulation calculating qubit frequency at the ε_L (yellow histogram) and ε_R (green histogram) readout operating points. Black curves show Gaussian fits to the histograms.

F. Qubit frequency at the readout operating points

With all QDHQ parameters estimated, the qubit frequency ω_q can be calculated by diagonalizing the Hamiltonian in Eq. (S2). Figure S4(b) plots ω_q as a function of ε . For our work, we are particularly interested in the qubit frequency at the readout operating points marked by green and yellow circles in the plot. Using the Hamiltonian parameters for the Fig. 2 measurements found above, we compute $\omega_q/2\pi = 21.2 \pm 1.2$ GHz at the ε_L readout point and $\omega_q/2\pi = 31.9 \pm 3.1$ GHz at the ε_R readout point.

The qubit frequency uncertainties are obtained through a Monte Carlo simulation. In each simulation iteration, Hamiltonian parameter entries are drawn from Gaussian distributions whose means and standard deviations correspond to the values and uncertainties computed in previous sections. Figure S4(c) charts histograms of the readout-point qubit frequencies after 10,000 iterations. The frequency uncertainties are extracted through Gaussian fits to the histograms.

SIII. PARAMETER TABLE

TABLE S1. Summary of device and measurement parameters used throughout this work. Parameters are classified into one of three categories: ‘controlled’ variables with values chosen as part of the experiment protocol; ‘measured’ values determined primarily through direct measurement; and ‘calculated’ values determined primarily through a numerical calculation or simulation described in previous sections.

Resonator properties	Determination	Value	Units
Fundamental-mode frequency, $\omega_r/2\pi$	measured	1.30380	GHz
Photon decay rate, $\kappa/2\pi$	measured	124.5 ± 0.5	kHz
Loaded quality factor, Q_L	measured	$10,476 \pm 46$	
Characteristic impedance, Z_r	calculated	575	Ω
Charge-photon coupling rate, $g_c/2\pi$	calculated	3.16 ± 0.55	MHz
DQD properties			
P2-left dot lever arm, α_{P2}^L/h	measured	33.9 ± 1.2	GHz/mV
P3-right dot lever arm, α_{P3}^R/h	measured	36.0 ± 0.7	GHz/mV
P3 detuning lever arm, α_{P3}^E/h	measured	25.4 ± 1.2	GHz/mV
Coupling-gate detuning lever arm, α_C^E/h	measured	5.6 ± 1.0	GHz/mV
Electron temperature, T_e	measured	213 ± 6	mK
Fig. 1(c)			
Pulse peak-to-peak voltage amplitude, V_{pulse}	controlled	1.7	mV
Pulse-sequence high-voltage period, t_+	controlled	15	ns
Pulse-sequence low-voltage period, t_-	controlled	2	ns
Pulse-sequence duty cycle, D	controlled	0.88	
Pulse-sequence repetitions per data point	controlled	8.8×10^6	
Interdot singlet-singlet tunnel coupling, Δ_1/h	measured	7.3 ± 0.6	GHz
Right-dot tunneling resonance voltage splitting, V_R	measured	0.97 ± 0.03	mV
Right-dot singlet-triplet splitting, E_R/h	measured	34.8 ± 1.2	GHz
Minimum qubit frequency, $\omega_q(\varepsilon_0 = 0)/2\pi$	calculated	14.6 ± 1.2	GHz
Maximum qubit frequency, $\omega_q(\varepsilon_0 \gg 0)/2\pi$	calculated	34.8 ± 1.2	GHz
Figs. 2(b, c, d, e)			
Pulse detuning amplitude (b, c), $ \varepsilon_{\text{pulse}} /h$	controlled	63.5	GHz
Pulse detuning amplitude (d, e), $ \varepsilon_{\text{pulse}} /h$	controlled	0 to 63.5	GHz
Pulse phase period, $t_{\text{pulse}} (= t_-)$	controlled	2	ns
Measurement phase period, $t_{\text{meas}} (= t_+)$	controlled	48	ns
Pulse-sequence duty cycle, D	controlled	0.96	
Pulse-sequence repetitions per data point (b, c)	controlled	4×10^6	
Pulse-sequence repetitions per data point (d, e)	controlled	2×10^6	
Interdot singlet-singlet tunnel coupling, Δ_1/h	measured	4.4 ± 0.2	GHz
Interdot singlet-triplet tunnel coupling, Δ_2/h	measured	7.5 ± 0.6	GHz
Interdot singlet-triplet tunnel coupling, Δ_3/h	measured	6.1 ± 0.5	GHz
Interdot singlet-singlet tunnel coupling, Δ_4/h	calculated	9.3 ± 1.8	GHz
Left-dot singlet-triplet splitting, E_L/h	calculated	27.3 ± 1.0	GHz
Right-dot tunneling resonance voltage splitting, V_R	measured	1.15 ± 0.08	mV
Right-dot singlet-triplet splitting, E_R/h	measured	41.3 ± 2.9	GHz
$ 1\rangle$ - $ 2\rangle$ anticrossing detuning, ε_L/h	measured	-24.0 ± 1.0	GHz
$ 1\rangle$ - $ 2\rangle$ anticrossing detuning, ε_R/h	measured	36.7 ± 1.5	GHz
Minimum qubit frequency, $\omega_q(\varepsilon_0 = 0)/2\pi$	calculated	8.8 ± 0.4	GHz
Maximum qubit frequency, $\omega_q(\varepsilon_0 \gg 0)/2\pi$	calculated	41.3 ± 2.9	GHz
Readout-point qubit frequency, $\omega_q(\varepsilon_0 = \varepsilon_L)/2\pi$	calculated	21.2 ± 1.2	GHz
Readout-point qubit frequency, $\omega_q(\varepsilon_0 = \varepsilon_R)/2\pi$	calculated	31.9 ± 3.1	GHz

SIV. EXPERIMENTAL SETUP

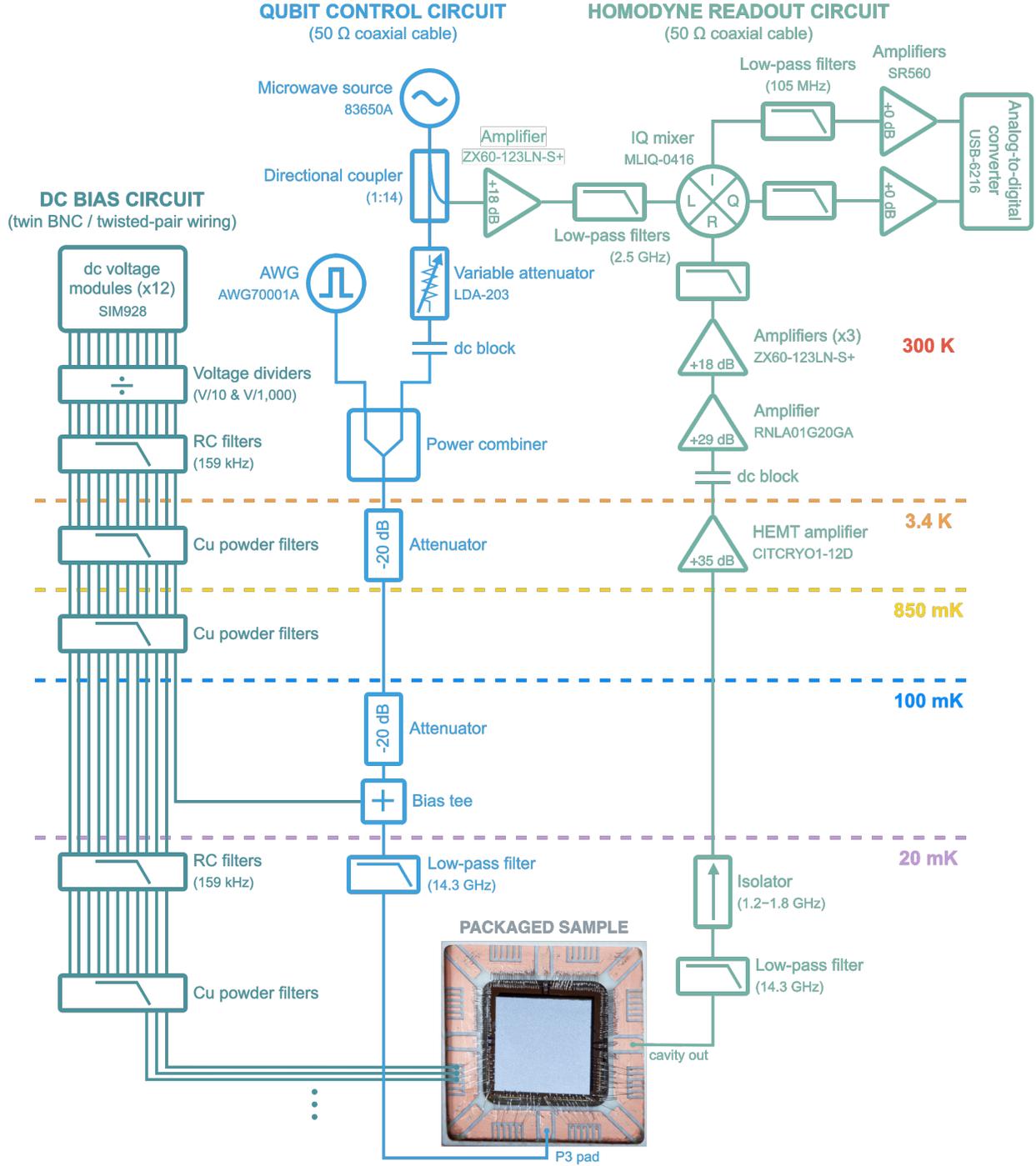


FIG. S5. Wiring diagram for the measurement instrumentation. Experiments are performed in a Leiden Cryogenics CF-450 dilution refrigerator with a mixing-chamber base temperature around 20 mK.